

A new method for simulating the motion of individual ellipsoidal bacteria in microfluidic devices†‡

Min-Cheol Kim^a and Catherine Klapperich^{*ab}

Received 25th February 2010, Accepted 7th May 2010

DOI: 10.1039/c003627g

To successfully perform biological experiments on bacteria in microfluidic devices, control of micron-scale cell motion in the chip-sized environment is essential. Here we describe a new method for simulating the motion of individual bacterial cells in a microfluidic device using a one-way coupling Lagrangian approach combined with rigid body theory. The cell was assumed to be an elastic, solid ellipsoid, and interactions with solid wall boundaries were considered to occur in one of two collision modes, either a “standing” or “lying” collision mode on the surface. The ordinary differential equations were solved along the cell trajectory for the thirteen unknown variables of the translational cell velocity, cell location vector, rotational angular velocity, and four Euler parameters, using the Rosenbrock method based on an adaptive time-stepping technique. As selected applications, we show how this novel simulation method may be applied to the designs of efficient hydrodynamic cell traps in a microfluidic device for bacterial applications and for cell separations. Modeled designs include optimized U-shaped sieve arrays with a single aperture for the hydrodynamic cell trapping, and three kinds of staggered micropillars for cell separations.

Introduction

Using microfluidic devices for the spatial localization of individual bacteria has the potential to impact research in many areas including systems biology, biosensors and biofuel cells.^{1–4} Consequently, there has been a growing interest in the design of microfluidic devices for immobilizing,² separating,⁵ and applying physical forces to bacteria. These include dielectrophoresis,⁶ optical traps,^{7,8} and hydrodynamic traps.⁹ Microfluidic technologies that can manipulate individual cells have the potential to lower reagent costs, enable larger experiment sets, and allow for faster reaction times compared to conventional bench top methods. Much of the modeling in this area has been focused on mammalian cells, which are well approximated as spherical particles when they are in suspension. Here we focus on modeling and predicting elliptical cell motion in devices aimed at cell trapping and sorting.

Optimal performance of living cell microfluidic devices can be achieved if computational tools are employed at the design stage.¹⁰ To date most commercial computational tools allow for fluid simulations that predict the pressure drop along the overall device, and the low and high fluid shear stresses acting on the cell.¹¹ Dynamic cell simulations in microfluidic devices are less common due to a lack of suitable computational tools. Dynamic cell simulations using Lagrangian modeling have recently been applied to the design of efficient hydrodynamic cell traps for

spherical mammalian cells in microfluidic devices.¹⁰ For dynamic cell simulations of bacteria in microfluidic devices, the computational approach of dynamic spherical cell simulations is lacking because hydrodynamic shear stress influences motion by biasing the non-spherical bacterium's direction.^{12–14} Thus, there is a need for a new method to simulate the motion of individual ellipsoidal bacteria in microfluidic devices for bacterial applications.

Hydrodynamic forces and torques acting on prolate spheroids in unbounded shear flow have been extensively studied to predict the motion of the spheroids.^{15–17} This work was extended to simulate aerosol particles in shear flow by incorporating the rigid body (RB) theory.¹⁸ Here we further develop this computational method of Lagrangian approach and RB theory to simulate different cell phenotypes (spherical and ellipsoidal shapes) and to visualize their motion in a microfluidic device for observations on the order of microseconds. The computational method presented has been demonstrated for the problem of trapping mammalian cells in a sieve based microfluidic trapping device and showed good agreement with on-chip cell trapping experiments.¹⁰ The current report shows how this method can be applied to ellipsoidal cells in both a trapping and a sorting device.

Methods

Ellipsoidal *Escherichia coli* modeling

The motion of ellipsoidal *E. coli* in the microfluidic devices was simulated using a Lagrangian approach based on one-way coupling between the time dependent particle motion and the pre-computed Newtonian flow fields. In fluid mechanics, Lagrangian is described as a way of looking at fluid motion where the observer follows an individual fluid parcel as it moves through space and time. Detailed methods for constructing computational geometric models from 2D CAD drawings and computing the flow fields in microfluidic devices are found in the

^aDepartment of Biomedical Engineering, Boston University, Boston, MA, 02215, USA. E-mail: catherin@bu.edu

^bDepartment of Mechanical Engineering, Boston University, Boston, MA, 02215, USA

† Published as part of a special issue dedicated to Emerging Investigators: Guest Editors: Aaron Wheeler and Amy Herr.

‡ Electronic supplementary information (ESI) available: Three movies of bacteria in a microfluidic device with circular micro-posts and C++ code enabling replication of the simulations. See DOI: 10.1039/c003627g

literature.¹⁰ The calculations interpolate the flow velocity and velocity gradients at the cell body's center of mass. A microbial cell was assumed to be an elastic ellipsoid with a major length of 4 μm and a minor length of 1 μm . Interactions between moving cells were not considered because the suspension was of a sufficiently low concentration. However, interactions with the channel's surface were considered to both prohibit moving cells from penetrating the computational wall boundary and to describe tumbling motions of *E. coli* on the surface. The forces considered in the equation of translational motion for an ellipsoidal cell were those due to the hydrodynamic drag, pressure gradient, gravity, Brownian motion and collisions between cells and the surface. In addition, the torques considered in the equations of rotational motion for the ellipsoidal cells were hydrodynamic torque and repulsive torques induced by collisions with cells already stuck on the surface. The resulting translational motion equations for the ellipsoidal cell are expressed as:

$$m_p \frac{d\mathbf{u}_p^*}{dt} = \mathbf{F}_H + \mathbf{F}_{PG} + (m_p - m_f)\mathbf{g} + \mathbf{F}_B + \mathbf{F}_S + \mathbf{F}_W \quad (1)$$

$$\frac{d\mathbf{x}_p^*}{dt} = \mathbf{u}_p^* \quad (2)$$

where \mathbf{u}_p^* is the particle velocity, \mathbf{x}_p^* is the location vector, and $\mathbf{F}_H (= \pi a \mu \tilde{\mathbf{K}}(\mathbf{u}_f - \mathbf{u}_p^*))$ is the hydrodynamic drag force acting on the ellipsoidal cell under the Stokes flow regime expressed as only the first term of an infinite series of fluid velocity and its spatial

derivatives.¹⁵ Here \mathbf{u}_f stands for fluid velocity at the center of mass (\mathbf{x}_p^*), μ is the dynamic viscosity of fluid ($8.88 \times 10^{-3} \text{ kg m}^{-1} \text{ s}^{-1}$), and $m_p (= 4\pi a^3 \beta \rho_p / 3)$ and $m_f (= 4\pi a^3 \beta \rho_f / 3)$ are the mean masses of the ellipsoidal particle and fluid, respectively. Here, $\beta (= b/a)$ is the ellipsoidal aspect ratio of semi-major (b) and semi-minor (a) axes, and ρ_p and ρ_f are particle density (1040 kg m^{-3}) and fluid density (997.5 kg m^{-3}), respectively. $\tilde{\mathbf{K}}$ is a translation tensor, and is expressed as the following:

$$\tilde{\mathbf{K}} = \mathbf{R}^{-1} \hat{\mathbf{K}} \mathbf{R} \quad (3)$$

where the matrix \mathbf{R} transforms the motion-frame system ($\hat{x}_1, \hat{x}_2, \hat{x}_3$) into the body-frame system ($\hat{x}_1, \hat{x}_2, \hat{x}_3$) in terms of Euler's four parameters (quaternion; $\varepsilon_1, \varepsilon_2, \varepsilon_3, \eta$)²⁰ or the Euler angles (θ, ϕ , and ψ)²¹ (see Fig. 1A and B), and is written as

$$\mathbf{R} = \begin{pmatrix} 1 - 2(\varepsilon_2^2 + \varepsilon_3^2) & 2(\varepsilon_1\varepsilon_2 + \varepsilon_3\eta) & 2(\varepsilon_1\varepsilon_3 - \varepsilon_2\eta) \\ 2(\varepsilon_2\varepsilon_1 - \varepsilon_3\eta) & 1 - 2(\varepsilon_3^2 + \varepsilon_1^2) & 2(\varepsilon_2\varepsilon_3 + \varepsilon_1\eta) \\ 2(\varepsilon_3\varepsilon_1 + \varepsilon_2\eta) & 2(\varepsilon_3\varepsilon_2 - \varepsilon_1\eta) & 1 - 2(\varepsilon_1^2 + \varepsilon_2^2) \end{pmatrix}, \quad (4)$$

$\hat{\mathbf{K}}$ is the body-frame's diagonal matrix for the revolution of the ellipsoidal particle along the \hat{x}_2 -axis; its diagonal elements, \hat{K}_{11} , \hat{K}_{22} , and \hat{K}_{33} represent hydrodynamic drag coefficients on the ellipsoidal particle in the flow fields of the body frame,¹⁶ and expressed as

$$\hat{K}_{11} = \hat{K}_{33} = 16(\beta^2 - 1) \left/ \left[\frac{2\beta^2 - 3}{\sqrt{\beta^2 - 1}} \ln(\beta + \sqrt{\beta^2 - 1}) + \beta \right] \right.$$

$$\text{and } \hat{K}_{22} = 8(\beta^2 - 1) \left/ \left[\frac{2\beta^2 - 1}{\sqrt{\beta^2 - 1}} \ln(\beta + \sqrt{\beta^2 - 1}) - \beta \right] \right., \quad (5)$$

and \mathbf{F}_{PG} , the force due to the pressure gradient in the fluid surrounding the particle, is given as:

$$\mathbf{F}_{PG} = -V_p \nabla p \approx m_f \frac{D\mathbf{u}_f}{Dt} \approx \frac{4}{3} \pi a^3 \beta \rho_f \frac{\mathbf{u}_f^1 - \mathbf{u}_f^0}{dt} \quad (6)$$

where D/Dt is the material derivative which describes the time rate of change of momentum, while moving with a space and time dependent velocity field, \mathbf{u}_f^0 denotes the fluid velocity vector at the previous time and \mathbf{u}_f^1 denotes the velocity vector at the present time, which is evaluated at the estimated position ($\mathbf{x}_p^1 = \mathbf{x}_p^0 + dt\mathbf{u}_p^0$).¹⁹ The pressure gradient term, representing the fluid inertia, is approximated by the material derivative of the acceleration of a fluid element, neglecting the viscous terms in the Navier–Stokes equation. In addition, both the inertia of the fluid and of the particle itself cause rotation of the ellipsoidal particle with its long axis perpendicular to the vorticity of the flow under the maximum Reynolds number of about 10^{-3} .²² To consider the effective elastic interactions between non-spherical cells, an ellipsoidal cell model was constructed from 32 elastic beads (see Fig. 1C). Elastic collisions between moving cells and deposited cells were modelled using a spring force, \mathbf{F}_S , expressed by:

$$\mathbf{F}_S = \begin{cases} 0 & \text{if } d_{km} > d_b \\ \sum_{i \neq j}^N \left(\sum_{k=1}^{32} \left(\sum_{m=1}^{32} (k_p(d_b - d_{km})) \right) \right) \hat{n}_{km} & \text{if else } d_{km} \leq d_b \end{cases} \quad (7)$$

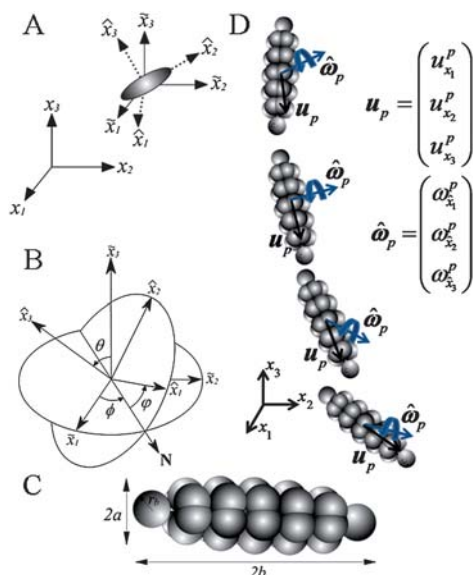


Fig. 1 (A) Schematic of an ellipsoidal cell moving in a global coordinate system (x_1, x_2, x_3), the body-frame ($\hat{x}_1, \hat{x}_2, \hat{x}_3$), and the motion-frame ($\hat{x}_1, \hat{x}_2, \hat{x}_3$), (B) Euler angles; N is the line of nodes, ϕ is the angle between the \hat{x}_1 -axis and the line of nodes, θ is the angle between the \hat{x}_3 -axis and the \hat{x}_2 -axis, and ϕ is the angle between the line of nodes and the \hat{x}_1 -axis, (C) computational model for an ellipsoidal *E. coli* cell with a semi-minor length, $a = 0.5 \mu\text{m}$, and a semi-major length, $b = 2 \mu\text{m}$, which is composed of thirty two beads with radius $r_b = 0.285 \mu\text{m}$ and can be constructed using the parameterized formulas: $x = a \sin \sigma \cos v$, $y = b \sin v$ and $z = a \cos \sigma \cos v$ where $0 \leq \sigma \leq 180$, $0 \leq v \leq 360$, and (D) a diagram showing translational velocities and rotational angular velocities at discrete times.

where k_p is the effective stiffness constant of the cell estimated from measurements on transformed cell lines (3.2×10^{-4} N m $^{-1}$),²³ d_b is the diameter of one of the elastic beads (0.57 μ m), d_{km} is the distance between center of cell i 's bead k and cell j 's bead m , \hat{n}_{km} is normal vector between cell i 's bead k and cell j 's bead m , and N is the total number of seeded cells in the computational domain. \mathbf{F}_B represents the Brownian random force, which is induced by collisions between microscale cell and fluid molecules. Using the Einstein relationship, the explicit expression for the diffusion of the ellipsoidal particle (D_i) in the \hat{x}_i direction is given as

$$D_i = \frac{k_B T}{K_{ii} \pi a \mu} \quad (8)$$

where k_B is the Boltzmann constant and T is the temperature of the medium. A Gaussian probability density function (PDF) for body-frame displacement ($\Delta \hat{x}_i$) with mean value ($\langle \Delta \hat{x}_i \rangle = 0$) and mean-square value ($\langle [\Delta \hat{x}_i]^2 \rangle = 2D_i \Delta t$) is expressed as

$$f(\Delta \hat{x}_i, \Delta t) = \frac{1}{\sqrt{4\pi D_i \Delta t}} \exp\left(-\frac{\Delta \hat{x}_i^2}{4D_i \Delta t}\right). \quad (9)$$

Brownian motion for the time step (Δt) in the \hat{x}_i direction can be evaluated using Gaussian random numbers.²⁴ Thus, the ellipsoidal cell's center of mass position is corrected by the particle-frame displacement ($\Delta \mathbf{x}$), which can be obtained by inverting the body-frame displacement ($\Delta \mathbf{x} = \mathbf{R}^{-1} \Delta \hat{\mathbf{x}}$).^{25,26} The rotational motion equations used to find the angular velocity ($\hat{\omega}_p^*$) of a particle are expressed in the body-space (see Fig. 1D):

$$\hat{I} \frac{d\hat{\omega}_p^*}{dt} = \hat{I} \hat{\omega}_p^* \times \hat{\omega}_p^* + \hat{T}_H + \hat{T}_W \quad (10)$$

where \hat{I} is moment of inertia diagonal matrix in the body frame with elements \hat{I}_{11} , \hat{I}_{22} , and \hat{I}_{33} about the principal axes. For the ellipsoidal particle, they are expressed as

$$\hat{I}_{11} = \hat{I}_{33} = 0.2(1 + \beta^2)a^2 m_p, \quad \hat{I}_{22} = 0.4a^2 m_p. \quad (11)$$

\hat{T}_H is the hydrodynamic torque acting on the ellipsoidal particle, and its elements (\hat{T}_1^H , \hat{T}_2^H , and \hat{T}_3^H) are expressed as¹²

$$\hat{T}_1^H = \frac{16\pi\mu a^3 \beta}{3(\beta^2 \beta_0 + \gamma_0)} \left[(\beta^2 - 1)\hat{d}_1^f + (\beta^2 + 1)(\hat{\omega}_1^f - \hat{\omega}_1^{*p}) \right] \quad (12a)$$

$$\hat{T}_2^H = \frac{32\pi\mu a^3 \beta}{3(\gamma_0 + \alpha_0)} (\hat{\omega}_2^f - \hat{\omega}_2^{*p}) \quad (12b)$$

$$\hat{T}_3^H = \frac{16\pi\mu a^3 \beta}{3(\beta^2 \beta_0 + \alpha_0)} \left[(1 - \beta^2)\hat{d}_3^f + (1 + \beta^2)(\hat{\omega}_3^f - \hat{\omega}_3^{*p}) \right] \quad (12c)$$

where ω_1^{*p} , ω_2^{*p} , and ω_3^{*p} are the particle angular velocities with respect to the principal axes, and

$$\begin{aligned} d_1^f &= 0.5 \left(\partial \hat{u}_3^f / \partial \hat{x}_2 + \partial \hat{u}_2^f / \partial \hat{x}_3 \right), \quad d_3^f = 0.5 \left(\partial \hat{u}_2^f / \partial \hat{x}_1 + \partial \hat{u}_1^f / \partial \hat{x}_2 \right) \\ \omega_1^f &= 0.5 \left(\partial \hat{u}_3^f / \partial \hat{x}_2 - \partial \hat{u}_2^f / \partial \hat{x}_3 \right), \quad \omega_2^f = 0.5 \left(\partial \hat{u}_1^f / \partial \hat{x}_3 - \partial \hat{u}_3^f / \partial \hat{x}_1 \right) \\ \omega_3^f &= 0.5 \left(\partial \hat{u}_2^f / \partial \hat{x}_1 - \partial \hat{u}_1^f / \partial \hat{x}_2 \right) \end{aligned} \quad (13)$$

are the elements of the deformation rate and the spin tensors. Here, \hat{u}_1^f , \hat{u}_2^f , and \hat{u}_3^f are elements of the fluid velocity in the body frame coordinates, and the dimensionless parameters in eqn (12) are given as²⁷

$$\begin{aligned} \alpha_0 &= \gamma_0 = \frac{\beta^2}{\beta^2 - 1} + \frac{\beta}{2(\beta^2 - 1)^{3/2}} \log \left(\frac{\beta - \sqrt{\beta^2 - 1}}{\beta + \sqrt{\beta^2 - 1}} \right), \\ \beta_0 &= -\frac{2}{\beta^2 - 1} - \frac{\beta}{(\beta^2 - 1)^{3/2}} \log \left(\frac{\beta - \sqrt{\beta^2 - 1}}{\beta + \sqrt{\beta^2 - 1}} \right) \end{aligned} \quad (14)$$

The velocity gradient in the body frame was obtained using the transformation $\hat{\mathbf{G}} = \mathbf{R} \mathbf{G} \mathbf{R}^{-1}$ where $\hat{\mathbf{G}}$ and \mathbf{G} denote dyadic matrices in the body and motion frames, respectively.

For the RB simulation, the time rate of change of the four Euler parameters (quaternions) is related to the particle angular velocity by

$$\begin{pmatrix} d\epsilon_1/dt \\ d\epsilon_2/dt \\ d\epsilon_3/dt \\ d\eta/dt \end{pmatrix} = 0.5 \begin{pmatrix} \eta & -\epsilon_3 & \epsilon_2 \\ \epsilon_3 & \eta & -\epsilon_1 \\ -\epsilon_2 & \epsilon_1 & \eta \\ -\epsilon_1 & -\epsilon_2 & -\epsilon_3 \end{pmatrix} \cdot \hat{\omega}_p^*. \quad (15)$$

Each ellipsoidal cell trajectory was computed by integrating the thirteen ordinary differential equations (eqn (1), (2), (10), and (15)) under the following initial conditions. The initial cell velocity was interpolated using the fluid velocity at the initial seeding location, and the initial cell angular velocity was set to zero. The orientation of the ellipsoidal cell was defined as a unit vector \hat{j} in the direction in the body frame. Initially, the global orientation was set to be parallel to the flow direction at the inlet region. To eliminate the singularity difficulty associated with using Euler angles, the initial conditions of the four Euler parameters were obtained using following formula¹⁸ for $\eta \neq 0$,

$$\begin{aligned} \eta &= \pm 0.5(1 + a_{11} + a_{22} + a_{33})^{1/2} \\ &= \pm 0.5[(1 + \cos \theta)(1 + \cos(\phi + \psi))]^{1/2}, \\ \begin{pmatrix} \epsilon_1 \\ \epsilon_2 \\ \epsilon_3 \end{pmatrix} &= \frac{1}{4\eta} \begin{pmatrix} a_{23} - a_{32} \\ a_{31} - a_{13} \\ a_{12} - a_{21} \end{pmatrix} = \frac{1}{4\eta} \begin{pmatrix} \sin \theta(\cos \phi + \cos \psi) \\ \sin \theta(\sin \phi - \sin \psi) \\ (1 + \cos \theta)\sin(\phi + \psi) \end{pmatrix} \end{aligned} \quad (16a)$$

For $\eta = 0$,

$$\begin{pmatrix} \epsilon_1 \\ \epsilon_2 \\ \epsilon_3 \end{pmatrix} = \left[\pm \sqrt{\frac{1 + a_{11}}{2}}, \begin{cases} \frac{a_{12}}{2\epsilon_1} \text{ for } \epsilon_1 \neq 0 \\ \pm \sqrt{\frac{1 + a_{22}}{2}} \text{ for } \epsilon_1 = 0 \end{cases}, \begin{cases} \frac{a_{23}}{2\epsilon_2} \text{ for } \epsilon_2 \neq 0 \\ \pm \sqrt{\frac{1 + a_{33}}{2}} \text{ for } \epsilon_2 = 0 \end{cases} \right]^T \quad (16b)$$

where a_{ij} , components of matrix \mathbf{R} (eqn (4)), are the direction cosines. The cell seeding concentration was set at 2×10^7 CFU mL $^{-1}$ at a bulk flow rate of 0.1 μ L min $^{-1}$. A fourth order Rosenbrock method based on a adaptive time-stepping technique was utilized as the integration method, as it was more reliable for solving stiff linear equations without divergence than the Runge–Kutta method.²⁸

In previous work, Kim *et al.* compensated for interactions between spherical cells and solid wall boundaries.¹⁰ For the spherical cells, the detection of these interactions in the near-wall region, where the height from the surface of solid boundaries to the center of the cell (h_p) is less than cell's radius is straightforward because there is a single value for the radius for any given spherical cell's surface. However, in the case of an ellipsoidal cell, the near-wall region was defined as the region where the height from the surface of solid boundary to the center of the cell is less than the length of the semi-major axis of the ellipsoidal cell ($h_p < b$) because of the non-uniform curvature depending on the ellipsoidal cell's position. The wall interaction force (F_w), which based on tangential friction on the wall, and torque (T_w) between the ellipsoidal cell and solid wall boundary exist only if the cell contacts the solid boundary. However, there is an exceptional case where contact does not occur between the cell and the solid boundaries even when the ellipsoidal cell is located within the near-wall region ($h_p < b$). For example, it moves without touching on the surface in case that h_p is more than the length of the semi-minor axis of the cell ($h_p > a$) its orientation is parallel to the wall boundary. On the other hand, when the ellipsoidal cell's orientation (\hat{n}_p^o , unit vector) is changed to tilt inward or outward from the boundary, cell contact with the wall will occur (Fig. 2). The determination of the contact of an ellipsoidal cell with the wall boundary was given by

$$\text{contact occurs, if } h_p \leq h_c = \sqrt{a^2 \sin^2 \theta_c + b^2 \cos^2 \theta_c} \left| \left(\hat{n}_w \cdot \hat{n}_p^c \right) \right| \quad (17)$$

where h_c is the vertically projected distance of the length from the contact point on the surface to the cell's center, \hat{n}_w is an inward pointing normal unit vector of the wall surface, \hat{n}_p^c is contact unit vector of the cell body, and θ_c is the angle between \hat{n}_p^o and \hat{n}_p^c . To offset interactions between the ellipsoidal cells and solid wall boundaries, inward vertical bead velocity (U_b) and geometric correction factor (δ_b) were defined as follows:

$$U_b = \begin{cases} |\mathbf{u}_p^* \cdot \hat{n}_w| & \text{if } \mathbf{u}_p^* \cdot \hat{n}_w < 0 \\ 0 & \text{else,} \end{cases} \quad (18)$$

$$\delta_b = \begin{cases} 1.5(r_b - h_b) & \text{if } h_b < r_b \\ 0 & \text{else,} \end{cases} \quad (19)$$

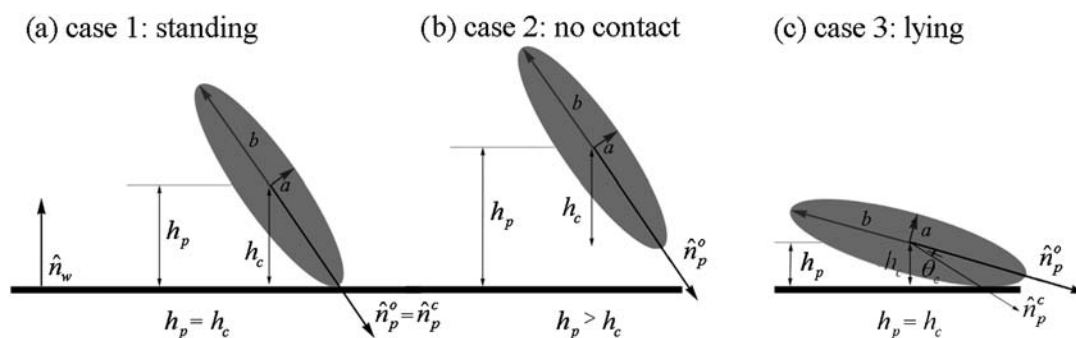


Fig. 2 Descriptions of ellipsoidal cell contacts on the surface at solid boundaries: (A) the standing collision mode, (B) no contact and (C) a cell in the lying collision mode.

where \mathbf{u}_p^* is the predicted cell velocity obtained from eqn (1) and (2) and h_b is the distance from the center of the bead to the wall surface. Thus, the velocity, position, and angular velocity vectors in the near-wall region were corrected as

$$\mathbf{u}_p = \mathbf{u}_p^* - U_b \hat{n}_w \quad (20)$$

$$\mathbf{x}_p = \mathbf{x}_p^* + \delta_b \hat{n}_w \quad (21)$$

$$\hat{\omega}_p = \hat{\omega}_p^* - \hat{I}^{-1} \mathbf{R}(\mathbf{r}_c \times m_p U_b \hat{n}_w) \quad (22)$$

Results and discussion

Ellipsoidal *E. coli* cell motion

Fig. 3 shows the selected continuous motion streams and streamlines of ellipsoidal *E. coli* cells in the top view. Longer intervals between cell motion streams indicate higher cell speed, and are observed at both the entrance and exit of the chamber. When the cells were loaded into the microchamber, the initial orientation of the cell was set to the negative y -direction, parallel to the flow direction at the inlet. The tumbling motions were

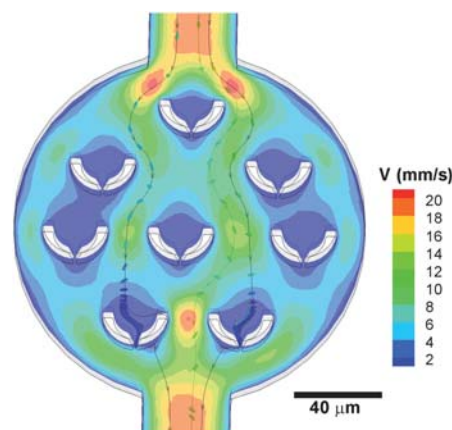


Fig. 3 An application of computational modelling to the design of microfluidic device for trapping bacteria in an aperture in a sieve; overlaid figure shows fluid velocity magnitude contours at the mid-section ($x_3 = 10 \mu\text{m}$), selected streamlines and bacteria's time-lapse trajectories. Here, V indicates velocity magnitude of both fluid and bacteria.

observed as they moved close to the solid wall boundaries. Additionally, as the cell approached the sieve, it decelerated due to increased hydrodynamic resistance and stagnation flow around the sieve. The undisturbed region of the stagnation point was located on the horizontal line between the two end tips of the U-type sieve. Interestingly, cell orientations were found to be almost parallel to the stagnation plane. Particles that entered the device parallel to the direction of flow all exhibited similar orientations as they flowed through the device. However, the trajectory of an ellipsoidal particle is strongly dependent on its initial orientation as it enters vortices; for instance, when an ellipsoidal particle enters a stagnation flow region and its initial orientation is 45° from the flow direction, it moves further away from the stagnation point (center) than a cell whose initial orientation as parallel to the principal directions of the flow field. This observation may facilitate a better understanding of the cell trapping conditions.

The computational modeling approach in the microfluidic device was also applied to evaluate the optimal design for sorting bacteria by their sizes. Each panel in Fig. 4 shows the continuous motion streams of three kinds of single *E. coli* cells ($\beta = 1$, $\beta = 2$ and $\beta = 4$) in the top and side views. Here, the three designs represent the evolution of the cross-sectional shape of the micropillar, from a circle to a tilted oval. In particular, the circular micropillar shown in Fig. 4A has previously been introduced to separate large sized spherical cells ($>2.3 \mu\text{m}$) from whole blood cells by employing collisional biophysics between the spherical cell body and the staggered micropillar arrays.²⁹ However, the design of the circular shaped micropillar shows incompatibility with ellipsoidal cells, as all three types of cells tend to slip along the post. These slip motions can be explained by the low aspect ratio of the semi-minor length of ellipsoidal cell (a) and the radius of the post,

resulting in insufficient impact against the post to push the cell laterally (Movie 1, ESI†).

To increase the cell's impact against the post, the second design of the micropillar was intended to increase its volume by increasing its aspect ratio in the diagonal direction of the desired cell motion. However, the simulated result shows lateral motion only when the polar tip of the ellipsoidal cell collides with the lateral surface of the post (standing mode in Fig. 2). Unfortunately, the rest of the continuous motion streams show sliding motions around the post. This is because the contact area between the ellipsoidal cell and oval shaped micropillar occurs at the surface close to the major axis of the post, resulting in insufficient torque to flip the ellipsoidal cell (or to change its orientation) toward to the diagonal direction (Movie 2, ESI†).

The third design of the micropillar array is further rotated in the counter-clockwise direction to increase the probability of a collision on the surface close to minor axis of the post. As a result, the ellipsoidal cell ($\beta = 4$) moves further laterally with periodic changes of its orientation after several collisions in the lying collision mode (lying mode in Fig. 2) than the other two cell types of ellipsoid cell ($\beta = 2$) and spherical cell ($\beta = 1$) (Movie 3, ESI†).

It is important to note that the limiting values of diagonal elements, \hat{K}_{11} , \hat{K}_{22} and \hat{K}_{33} in eqn (5) are equally 6, and the limiting values of α_0 , β_0 and γ_0 in eqn (14) are identically $2/3$ when β approaches one (spherical shape). Thereafter, hydrodynamic drag force in eqn (1) and torque in eqn (12) become exact forms of Stoke drag ($\mathbf{F}_H = 6\pi a\mu(\mathbf{u}_f - \mathbf{u}_p^*)$) and torque ($\hat{\mathbf{T}}_H = 8\pi a^3\mu(\boldsymbol{\omega}_f - \boldsymbol{\omega}_p^*)$) for the spherical particle. In particular, when β is less than one, the shape of particle become circular thin disk (red blood cell), and detailed information regarding coefficients of hydrodynamic force and torque for the circular disk ($\beta < 1$) are theoretically derived in the literature (Table 1).¹⁶

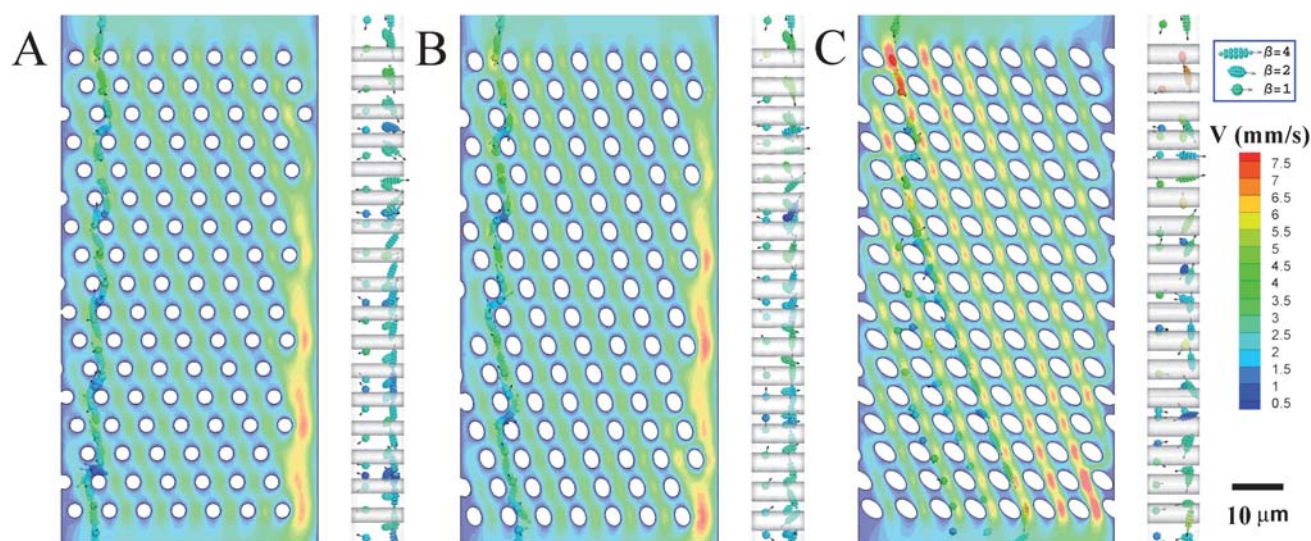


Fig. 4 Applications of computational bacteria cell modelling to the design of microfluidic device for sorting by size using three designs of staggered micro-posts: (A) circular micro-posts, (B) oval shaped micro-posts (tilted in diagonal direction) and (C) oval shaped micro-posts (further rotated in the counter-clockwise direction than (B)). The left of each panel shows fluid velocity magnitude contours at the mid-section ($x_3 = 5 \mu\text{m}$) and selected continuous motion streams of three kinds of bacterial shapes ($\beta = 1$, $\beta = 2$ and $\beta = 4$), and an arrow anchored in the cell center indicates the bacterial orientation. The right of each panel (vertical cross-section) shows variations of bacterial orientations during their motions where \mathbf{x}_p^* is the predicted particle position vector and $\boldsymbol{\omega}_p^*$ is the predicted particle angular velocity vector solved from eqn (10).

Table 1 List of simulation parameters

Parameter	Definition	Equation
D_i	Diffusion of the ellipsoidal particle	(8)
F	Force	(1) and (6)–(8)
G	Dyadic matrix in the body-frame	(13)
\bar{G}	Dyadic matrix in the motion-frame	(13)
I	Moment of inertia diagonal matrix in the body-frame	(10)
I_{ii}	i 's diagonal element in I	(11)
\bar{K}	Translation tensor in motion-frame	(3)
K	Body-frame's diagonal matrix	(3)
K_{ii}	i 's diagonal element in \bar{K}	(5)
R	Transformation matrix	(3), (4), and (22)
T	Torque in body-frame system	(10)
T_i	i 's element in T	(12)
U_b	Inward vertical bead velocity	(18)
V_p	Volume of ellipsoidal particle	(6)
a	Semi-minor length of ellipsoidal cell	(1), (6), (8), (11), and (17)
a_{ij}	i 's components of matrix R	(4)
b	Semi-major length of ellipsoidal cell	(17)
d_b	Diameter of one of the elastic beads	(7)
d_{km}	Distance between center of i 's bead k and cell j 's bead m	(7)
d_i^t	i 's element of fluid deformation tensor	(13)
dt	Adaptive time step	(6)
g	Gravitational vector	(1)
h_c	Vertically projected distance of the length from the contact point on the surface to the cell's center	(17)
h_p	Height from the surface to cell's center	(17)
k_p	Effective stiffness constant of the cell	(7)
m	Mass	(1), (6), (11), and (22)
\hat{n}_p^c	Contact unit vector of the cell body	(17)
\hat{n}_p^o	Cell's orientation unit vector	(17)
\hat{n}_w	Inward normal unit vector at the wall	(17), (18), and (20)–(22)
r	Radius	Fig. 1C and (19)
t	Time	(1), (2), (10), and (15)
u	Velocity vector	(1)
x	Location vector	(2)
x_1, x_2, x_3	Global coordinate system	(1) and (2)
$\hat{x}_1, \hat{x}_2, \hat{x}_3$	Body-frame coordinate system	(5), (10), (12), (15), and (22)
$\tilde{x}_1, \tilde{x}_2, \tilde{x}_3$	Motion-frame coordinate system	(3) and (13)
β	b/a , ellipsoidal aspect ratio	(1), (5), (6), (12), and (14)
$\alpha_0, \beta_0, \gamma_0$	Coefficients of hydrodynamic torque	(14)
δ_b	Geometric correction factor	(19)
$\varepsilon_1, \varepsilon_2, \varepsilon_3, \eta$	Euler's four parameters, quaternion	(4), (15), and (16)
μ	Dynamic viscosity of fluid	(1) and (8)
ρ_f	Fluid density	(1)
ρ_p	Particle density	(1)
θ, ϕ, ψ	Euler's angles	Fig. 1A and (16a)
θ_c	Angle between \hat{n}_p^c and \hat{n}_p^o	Fig. 2C and (17)
σ, v	Angles for ellipsoidal geometry	Fig. 1C
Subscript		
b	Bead	(7) and (19)
f	Fluid	(1), (6), (12), and (13)
p	Particle	(1), (2), (10), and (20)–(22)
H	Hydrodynamic force or torque	(1), (5), (10), and (12)
B	Brownian force	(1), (8), and (9)
PG	Pressure gradient	(1) and (6)
S	Spring elastic force	(1) and (7)
W	Wall interaction force or torque	(1), (10), and (17)–(22)
Superscription		
f	Fluid	(13)
p	Particle	(1)
0	Previous time	(6)
1	Present time	(6)
*	Estimated value	(1), (2), (10), (15), (18) and (20)–(22)

Current simulation method includes inertial effects of both fluid and particle phases by setting the left hand side term ($m_p d\mathbf{u}_p^*/dt$) and the pressure gradient term (F_{PG}) in eqn (1) although most commonly these inertial effects have been ignored due to misunderstanding of low Reynolds number (Re) in the

microfluidic channel.³⁰ For example, swimming *E. coli* occurs at very low Reynolds numbers ($Re \approx 10^{-4}$), and those works have ignored these inertial effects. However, flow speed of the bacteria in our model is much higher than swimming speed of *E. coli* ($Re \approx 10^{-2}$), and bacteria cell's decelerating feature around the

U-shaped sieves is observed due to inertial effects (see two trapping motions in Fig. 3).

In terms of computer requirements for solving current examples, Intel Core 2 Duo CPU with 1.67 GHz and 4 GB memory were utilized to build and solve computational grids whose number is less than 1000k. Grid sizes were set to fit with simulating bacteria size. For example, in the case of bacteria size of 1 μm by 4 μm , minimum and maximum grid sizes are empirically found to be 2 μm and 5 μm , respectively.

Current dynamic cell simulations were carried out using Rosenbrock method for integrating stiff ordinary differential equations with the convergence criterion $< 10^{-4}$. For example, eqn (1) is a stiff equation as its simplified form is expressed as $\text{d}\mathbf{u}_p^*/\text{d}t = -1.54 \times 10^7 \mathbf{u}_p^* + \sim$ for $\beta = 1$. Rosenbrock method is ideal for solving dynamic cell simulations rather than common Runge–Kutta method which requires to run relatively large number of iterations to avoid any further deviation.²⁸ Furthermore, Rosenbrock method consumes less time in computing by adaptive time-step control which ranges from 10^{-8} to 10^{-6} in this report.

Inter-bacteria collision was considered only when moving bacteria collide with stationary bacteria on the surface. However, inter-bacteria collision between moving bacteria occurs at higher cell density $> 10^8$ to 10^9 CFU mL^{-1} . In that case, some bacteria can bind with each other during their motions, and an additional multi-body dynamics can be applied to linking multi-bacteria components. One-way coupled Lagrangian approach is utilized under the condition of the dilute bacteria density of $< 10^8$ CFU mL^{-1} . For example, the number of bacteria in the device is simply calculated as > 12 CFU in a trapping device (Fig. 3, dimensions: 80 μm (r) by 20 μm (h)). Probability of inter-bacteria collision during their motions is very low, and this number of bacteria does not affect flow field in the device much. Thus, one-way coupled Lagrangian is valid in this range of cell density. However, in the case of bacteria density of $> 10^9$ CFU mL^{-1} , many number of bacteria > 120 CFU in the identical volume of the device is calculated, which results in high probability of inter-bacteria collision.

Conclusions

A novel simulation method to model the motion of ellipsoidal cells in microfluidic flow has been presented. The model combines RB motion with a one-way coupled Lagrangian approach between particle motion and flow fields. Trapping of simulated *E. coli* in sieve structures and sorting of *E. coli* in staggered micropillar arrays have been demonstrated as examples. Using this simulation method, we are able to predict the trapping and sorting performance in preliminary designs before prototyping. The sorting simulation results suggest that collisions closest to the minor axis of an oval shaped post are preferred to drive ellipsoidal cells laterally in the sorting device. In addition, the simulation method presented here could be further applied to solve for the motion of any axially symmetric cells including red and white blood cells.³¹

Acknowledgements

We acknowledge financial support from the Boston University Biosurfaces Initiative.

References

- 1 J. P. Bearinger, L. C. Dugan, L. Wu, H. Hill, A. T. Christian and J. A. Hubbell, Chemical tethering of motile bacteria to silicon surfaces, *BioTechniques*, 2009, **46**, 209–216.
- 2 C. J. Kastrup, J. Q. Boedicker, A. P. Pomerantsev, M. Moayeri, Y. Bian, R. R. Pompano, T. R. Kline, P. Sylvestre, F. Shen, S. H. Leppla, W.-J. Tang and R. F. Ismagilov, Spatial localization of bacteria controls coagulation of human blood by ‘quorum acting’, *Nat. Chem. Biol.*, 2008, **4**, 742–750.
- 3 A. Groisman, C. Lobo, H. J. Cho, J. K. Campbell, Y. S. Dufour, A. M. Stevens and A. Levchenko, A microfluidic chemostat for experiments with bacterial and yeast cells, *Nat. Methods*, 2005, **2**, 685–689.
- 4 R. H. W. Lam, M.-C. Kim and T. Thorsen, Culturing aerobic and anaerobic bacteria and mammalian cells with a microfluidic differential oxygenator, *Anal. Chem.*, 2009, **81**(14), 5918–5924.
- 5 Marcos, H. C. Fu, T. R. Powers and R. Stocker, Separation of microscale chiral objects by shear flow, *Phys. Rev. Lett.*, 2009, **102**, 158103.
- 6 L. Yang, P. P. Banada, M. R. Chatni, K. S. Lim, A. K. Bhunia, M. Ladisch and R. Bashir, A multifunctional micro-fluidic system for dielectrophoretic concentration coupled with immuno-capture of low numbers of *Listeria monocytogenes*, *Lab Chip*, 2006, **6**, 896–906.
- 7 A. Ashkin and J. M. Dziedzic, Optical trapping and manipulation of viruses and bacteria, *Science*, 1987, **235**, 1517–1520.
- 8 J. Enger, M. Goksör, K. Ramser, P. Hagberg and D. Hanstorp, Optical tweezers applied to a microfluidic system, *Lab Chip*, 2004, **4**, 196–200.
- 9 C. Lay, C. Y. Teo, L. Zhu, X. L. Peh, H. M. Ji, B.-R. Chew, R. Murthy, H. H. Feng and W.-T. Liu, Enhanced microfiltration devices configured with hydrodynamic trapping and a rain drop bypass filtering architecture for microbial cells detection, *Lab Chip*, 2008, **8**, 830–833.
- 10 M.-C. Kim, Z. Wang, R. H. W. Lam and T. Thorsen, Building a better cell trap: applying Lagrangian modeling to the design of microfluidic devices for cell biology, *J. Appl. Phys.*, 2008, **103**, 044701.
- 11 D. Di Carlo, L. Y. Wu and L. P. Lee, Dynamic single cell culture array, *Lab Chip*, 2006, **6**, 1445–1449.
- 12 G. B. Jeffrey, The motion of ellipsoidal particles immersed in a viscous fluid, *Proc. R. Soc. London, Ser. A*, 1922, **102**, 161–179.
- 13 G. M. Walker, J. Sai, A. Richmond, M. Stremmer, C. Y. Chung and J. P. Wikswo, Effects of flow and diffusion on chemotaxis studies in a microfabricated gradient generator, *Lab Chip*, 2005, **5**, 611–618.
- 14 Marcos and R. Stocker, Microorganisms in vortices: a microfluidic setup, *Limnol. Oceanogr.*, 2006, **4**, 392–398.
- 15 H. Brenner, The Stokes resistance of an arbitrary particle—IV arbitrary fields of flow, *Chem. Eng. Sci.*, 1964, **19**, 703–727.
- 16 J. Happel and H. Brenner, *Low Reynolds Number Hydrodynamics*, Springer, New York, 1st edn, 1981.
- 17 S. Kim and S. J. Karrila, *Microhydrodynamics: Principles and Selected Applications*, Butterworth-Heinemann, Boston, 1991.
- 18 F. G. Fan and G. Ahmadi, Dispersion of ellipsoidal particle in an isotropic pseudo-turbulent flow field, *J. Fluids Eng.*, 1995, **117**, 154–161.
- 19 M.-C. Kim, J. H. Nam and C. S. Lee, Near-wall deposition probability of blood elements as a new hemodynamics wall parameter, *Ann. Biomed. Eng.*, 2006, **34**, 958–970.
- 20 H. Goldstein, *Classical Mechanics*, Addison-Wesley, Reading, MA, 2nd edn, 1980.
- 21 P. C. Hughes, *Spacecraft Attitude dynamics*, Wiley, New York, 1986.
- 22 A. Karnis, H. Goldsmith and S. G. Mason, Particle motions in sheared suspension. Part 5. Inertial effects, *Can. J. Chem. Eng.*, 1966, **44**, 181.
- 23 W. A. Lam, M. J. Rosenbluth and D. A. Fletcher, Chemotherapy exposure increases leukemia cell stiffness, *Blood*, 2007, **109**, 3505–3508.
- 24 Y. Han, et al., Brownian motion of an ellipsoid, *Science*, 2006, **314**, 626–630.
- 25 D. Mukhija and M. J. Solomon, Translational and rotational dynamics of colloidal rods by direct visualization with confocal microscopy, *J. Colloid Interface Sci.*, 2007, **314**, 98–106.
- 26 B. Bhaduri, A. Neild and T. W. Ng, Directional Brownian diffusion dynamics with variable magnitudes, *Appl. Phys. Lett.*, 2008, **92**, 084105.

-
- 27 I. Gallily and A. H. Cohen, Orderly nature of the motion of nonspherical aerosol-particles. 2. Inertial collision between a spherical large droplet and an axially symmetrical elongated particle, *J. Colloid Interface Sci.*, 1979, **68**, 338–356.
- 28 W. H. Press, S. A. Teukolsky and B. P. Flannery, *Numerical Recipes in C*, Cambridge University Press, Cambridge, 1992.
- 29 D. W. Inglis, J. A. Davis, R. H. Austin and J. C. Sturm, Critical particle size for fractionation by deterministic lateral displacement, *Lab Chip*, 2006, **6**, 655–658.
- 30 D. Di Carlo, Inertial microfluidics, *Lab Chip*, 2009, **9**, 3038–3046.
- 31 C. Sun and L. L. Munn, Particulate nature of blood determines macroscopic Rheology: a 2-D lattice Boltzmann analysis, *Biophys. J.*, 2005, **88**, 1635–1645.